

# Universal halo mass function and scale-dependent bias from N-body simulations with non-Gaussian initial conditions

Annalisa Pillepich<sup>1\*</sup>, Cristiano Porciani<sup>1,2</sup> and Oliver Hahn<sup>1</sup>

<sup>1</sup>*Institute for Astronomy, ETH Zurich, 8093 Zurich, Switzerland*

<sup>2</sup>*Argelander Institut für Astronomie, Auf dem Hügel 71, D-53121, Germany*

10 April 2019

## ABSTRACT

We perform a series of high-resolution N-body simulations of cosmological structure formation starting from Gaussian and non-Gaussian initial conditions. We adopt the best-fitting cosmological parameters from the third- and fifth-year data releases of the *Wilkinson Microwave Anisotropy Probe* and we consider non-Gaussianity of the local type parameterised by 8 different values of the non-linearity parameter  $f_{\text{NL}}$ . Building upon previous work based on the Gaussian case, we show that, when expressed in terms of suitable variables, the mass function of friends-of-friends haloes is universal (i.e. independent of redshift, cosmology, and matter transfer function) to good precision also in non-Gaussian scenarios. We provide accurate fitting formulae for the high-mass end ( $M > 10^{13} h^{-1} M_{\odot}$ ) of the universal mass function in terms of  $f_{\text{NL}}$ . For Gaussian initial conditions, we extend our fit to a wider range of halo masses ( $M > 2.4 \times 10^{10} h^{-1} M_{\odot}$ ) and we also provide a consistent fit of the linear halo bias. We show that the matter power-spectrum in non-Gaussian cosmologies departs from the Gaussian one by several per cent on the scales where the baryonic-oscillation features are imprinted on the two-point statistics. Finally, using both the halo power spectrum and the halo-matter cross spectrum, we confirm the strong  $k$ -dependence of the halo bias on large scales ( $k < 0.05 h \text{ Mpc}^{-1}$ ) which was already detected in previous studies. However, we find that commonly used parameterisations based on the peak-background split do not provide an accurate description of our simulations which present extra dependencies on the wavenumber, the non-linearity parameter and, possibly, the clustering strength. We provide an accurate fit of the simulation data that can be used as a benchmark for future determinations of  $f_{\text{NL}}$  with galaxy surveys.

**Key words:** cosmology: theory, dark matter, large-scale structure – methods: N-body simulations – galaxies: haloes, clusters.

## 1 INTRODUCTION

The detection of temperature anisotropies in the Cosmic Microwave Background (CMB) provided evidence that large-scale structure formation in the universe was seeded by small density fluctuations generated at early times. The statistical properties of these seeds are usually modelled with a Gaussian random field. Historically the Gaussian approximation was introduced for mathematical convenience. In the absence of a solid model for the generation of density fluctuations the Gaussian hypothesis was accepted on the basis of the central limit theorem (e.g. Bardeen et al. 1986 and

references therein). The advent of inflationary models provided further support for Gaussianity. Small-amplitude curvature perturbations generated during a standard inflationary phase (single field, slow roll) are very nearly Gaussian distributed (e.g. Bartolo et al. 2004 and references therein).

However, many variants of the inflationary scenario predict appreciable levels of primordial non-Gaussianity. In terms of Bardeen’s gauge-invariant potential,  $\Phi$ , most of these models (but not all, see e.g. Creminelli et al. 2007) can be reduced to the form:

$$\Phi = \phi + f_{\text{NL}}(\phi^2 - \langle \phi^2 \rangle), \quad (1)$$

where  $\phi$  is an auxiliary Gaussian random field and  $f_{\text{NL}}$  quantifies the amount of primordial non-Gaussianity. On sub-

\* E-mail: annalisa@phys.ethz.ch

horizon scales,  $\Phi = -\Psi$  where  $\Psi$  denotes the usual peculiar gravitational potential related to density fluctuations via Poisson's equation. The parameter  $f_{\text{NL}}$  thus has the same sign as the skewness of the density probability distribution function. This local form of non-Gaussianity (note that equation (1) applies in configuration space) can be obtained from a truncated expansion of the effective inflaton potential (Salopek & Bond 1990; Falk et al. 1993; Gangui et al. 1994). The parameter  $f_{\text{NL}}$  thus encodes information about the inflaton physics. Standard inflation gives  $|f_{\text{NL}}| \ll 1$  (Salopek & Bond 1990; Maldacena 2003). However, even in this case, the non-linear evolution of perturbations on superhorizon scales yields an observable  $f_{\text{NL}}$  of order unity (which, in reality, should be scale and redshift dependent; Bartolo et al. 2005, see also Pyne & Carroll 1996). Large values of  $|f_{\text{NL}}|$  naturally arise in multi-field inflation models (e.g. Linde & Mukhanov 1997; for an extensive review see Bartolo et al. 2004 and references therein) and even in cyclic or ekpyrotic models of the universe with no inflation (Creminelli & Senatore 2007; Buchbinder et al. 2008; Lehnert & Steinhardt 2008).

Observational constraints on  $f_{\text{NL}}$  have been derived studying three-point statistics of temperature fluctuations in the CMB (Komatsu & Spergel 2001). The recent 5-year data from the *Wilkinson Microwave Anisotropy Probe* (WMAP) give  $-9 < f_{\text{NL}} < 111$  at the 95 per cent confidence level (Komatsu et al. 2008). Parallel studies on the same dataset give  $-178 < f_{\text{NL}} < 64$  using Minkowski functionals (Komatsu et al. 2008) and  $-8 < f_{\text{NL}} < 111$  from wavelet decomposition (Curto et al. 2008). Some recent reanalyses of earlier 3-year WMAP data claim substantial evidence for positive  $f_{\text{NL}}$ :  $27 < f_{\text{NL}} < 147$  from the bispectrum of temperature fluctuations (Yadav & Wandelt 2008) and  $23 < f_{\text{NL}} < 75$  from their one-point distribution function (Jeong & Smoot 2007). On the other hand, a study of Minkowski functionals on the 3-year data gives  $-70 < f_{\text{NL}} < 91$  (Hikage et al. 2008). Higher quality data are needed to improve these constraints. The upcoming Planck satellite should be able to reduce the uncertainty in  $f_{\text{NL}}$  to  $\sim 5$  (Komatsu & Spergel 2001).

Alternatively, one might use observational signatures of primordial non-Gaussianity imprinted in the large-scale structure (LSS) of the universe. Ideally, one would like to use high-redshift probes as the non-linear growth of density fluctuations quickly superimposes a strong non-Gaussian signal onto the primordial one so that the latter might then be difficult to recover. For instance, the large-scale distribution of neutral hydrogen in the era between hydrogen recombination and reionisation encodes information on  $f_{\text{NL}}$  (Pillepich et al. 2007). This could be probed by detecting the redshifted hyperfine 21-cm transition with very low-frequency radio arrays from space. In principle, an experiment of this kind can limit  $f_{\text{NL}}$  to  $\Delta f_{\text{NL}} < 1$  (Pillepich et al. 2007, see also Cooray 2006). However, it is not clear yet whether such an experiment will ever be possible due to technical complexity and problematic foreground subtraction. At lower redshifts,  $f_{\text{NL}}$  can be constrained probing the statistics of rare events, as like as the mass function of galaxy groups and clusters (Matarrese et al. 1986, 2000; Robinson & Baker 2000; Robinson et al. 2000; LoVerde et al. 2008). Early attempts of using cluster counts to constrain  $f_{\text{NL}}$  have been rather inconclusive due to low-

number statistics (see e.g. Willick 2000; Amara & Refregier 2004 and references therein). Even though cluster-mass estimates are still rather uncertain and massive objects are very rare, the observational perspectives look very promising. A number of galaxy surveys encompassing large fractions of the observable universe are being planned (e.g. ground-based surveys as DES, PanSTARRS, and LSST, and the satellite missions EUCLID and ADEPT) and could potentially lead to solid measurements of  $f_{\text{NL}}$  (e.g. Dalal et al. 2008; Carbone et al. 2008).

Primordial non-Gaussianity is also expected to modify the clustering properties of massive cosmic structures forming out of rare density fluctuations (Grinstein & Wise 1986; Matarrese et al. 1986; Lucchin et al. 1988). Also in this case, however, the non-linear evolution of the mass density generally superimposes a stronger signal than that generated by primordial non-Gaussianity onto the galaxy three-point statistics. The galaxy bispectrum is thus sensitive to  $f_{\text{NL}}$  only at high redshift (Verde et al. 2000; Scoccimarro et al. 2004; Sefusatti & Komatsu 2007).

Recently, Dalal et al. (2008) have shown analytically that primordial non-Gaussianity of the local type is expected to generate a scale-dependent large-scale bias in the clustering properties of massive dark-matter haloes. This is a consequence of the fact that large and small-scale density fluctuations are not independent when  $f_{\text{NL}} \neq 0$ . Similar calculations have been presented by Matarrese & Verde (2008), Slosar et al. (2008), Afshordi & Tolley (2008), and McDonald (2008). Numerical simulations by Dalal et al. (2008) are in qualitative agreement with the analytical predictions confirming the presence of a scale-dependent bias. Using these analytical models for halo biasing to describe the clustering amplitude of luminous red galaxies and quasars from the *Sloan Digital Sky Survey*, Slosar et al. (2008) obtained  $-29 < f_{\text{NL}} < 69$  at the 95 per cent confidence level. This shows that LSS studies are competitive with CMB experiments to constrain primordial non-Gaussianity but also calls for more accurate parameterisations of the mass function and clustering statistics of dark-matter haloes arising from non-Gaussian initial conditions.

Most of the analytic derivations of the non-Gaussian halo mass function are based on the extended Press-Schechter model (Press & Schechter 1974; Bond et al. 1991) which, in the Gaussian case, is known to produce inaccurate estimates of halo abundance (Sheth & Tormen 1999; Jenkins et al. 2001). Similarly, the scale dependent bias is obtained either using the peak-background split model (Slosar et al. 2008) or assuming that haloes form from the highest linear density peaks (Matarrese & Verde 2008). Both techniques have limited validity in the Gaussian case (Jing 1998; Porciani et al. 1999; Sheth & Tormen 1999). In this paper we test the accuracy of the excursion-set model and the peak-background split in the non-Gaussian case. This extends the previous studies of Kang et al. (2007) and Grossi et al. (2007) for the halo mass function and Dalal et al. (2008) for the halo bias by exploring more realistic values for  $f_{\text{NL}}$  with simulations of better quality. In practice, we run a series of high-resolution N-body simulations where we follow the process of structure formation starting from Gaussian and non-Gaussian initial conditions. The halo mass function and bias extracted from the simulations are then compared with the existing analytical models and

**Table 1.** Specifics of the N-body simulations.

Name	$f_{\text{NL}}$	$N_{\text{part}}$	$L_{\text{box}}$ ( $h^{-1}\text{Mpc}$ )	$M_{\text{part}}$ ( $h^{-1}M_{\odot}$ )	$L_{\text{soft}}$ ( $h^{-1}\text{kpc}$ )	$z_{\text{start}}$	Cosmology
1.270	+270	$1024^3$	1200	$1.246 \times 10^{11}$	20	50	WMAP5
1.180	+180	$1024^3$	1200	$1.246 \times 10^{11}$	20	50	WMAP5
1.90	+90	$1024^3$	1200	$1.246 \times 10^{11}$	20	50	WMAP5
1.30	+30	$1024^3$	1200	$1.246 \times 10^{11}$	20	50	WMAP5
1.10	+10	$1024^3$	1200	$1.246 \times 10^{11}$	20	50	WMAP5
1.0	0	$1024^3$	1200	$1.246 \times 10^{11}$	20	50	WMAP5
1.-10	-10	$1024^3$	1200	$1.246 \times 10^{11}$	20	50	WMAP5
1.-30	-30	$1024^3$	1200	$1.246 \times 10^{11}$	20	50	WMAP5
2.0	0	$1024^3$	1200	$1.072 \times 10^{11}$	20	50	WMAP3
2.270	+270	$1024^3$	1200	$1.072 \times 10^{11}$	20	50	WMAP3
3.0	0	$1024^3$	150	$2.433 \times 10^8$	3	70	WMAP5
3.90	+90	$1024^3$	150	$2.433 \times 10^8$	3	70	WMAP5

used to build accurate fitting formulae. These will provide a benchmark for future determinations of non-Gaussianity with galaxy surveys.

The paper is organised as follows. In Section 2 we describe our N-body simulations. In Sections 3, 4, and 5 we present our results for the halo mass function, the matter power spectrum and the halo bias, respectively. In Section 6 we discuss the implications of our results for the analysis by Slosar et al. (2008). Our conclusions are summarised in Section 7.

## 2 N-BODY SIMULATIONS

### 2.1 Specifics of the simulations

We use the lean version of the tree-PM code GADGET-2 (Springel 2005) kindly made available by Volker Springel to follow the formation of cosmic structure in a flat  $\Lambda$ CDM cosmology. We run three different series of simulations (each containing  $1024^3$  collisionless particles) that differ in the adopted cosmology, box size (and thus force softening length,  $L_{\text{soft}}$ ), and initial redshift (details are summarised in Table 1). The assumed cosmological parameters are listed in Table 2. For our series #1 and #3 they coincide with the 5-yr WMAP best estimates (Komatsu et al. 2008). The combined 3-yr WMAP+LSS results by Spergel et al. (2007) are instead used for series #2.

We produce non-Gaussian initial conditions directly applying equation (1) after having generated the Gaussian random field  $\phi$  with standard Fourier techniques. We consider 8 values for the parameter  $f_{\text{NL}}$ :  $-30, -10, 0, +10, +30, +90, +180, +270$  in agreement with the constraints from CMB data (Komatsu et al. 2008). Within each series of simulations, we use the same set of random phases to generate the Gaussian potential  $\phi$ . This facilitates the comparison between different runs by minimising sample variance.

The linear matter transfer function,  $T(k)$ , is computed using the LINGER code (Bertschinger 2001) and is applied after creating the non-Gaussian potential  $\Phi$  in equation (1). Particle displacements at  $z_{\text{start}}$  are generated using the Zel'dovich approximation (Zel'dovich 1970). Particle posi-

tions and velocities are saved for 30 time steps logarithmically spaced in  $(1+z)^{-1}$  between  $z = 10$  and  $z = 0$ .

Dark-matter haloes are identified using the standard friends-of-friends (FOF) algorithm with a linking length equal to 0.2 times the mean interparticle distance. We only considered haloes containing at least 100 particles.

Our first two series of simulations only include large periodic boxes covering a volume of  $(1200 h^{-1}\text{Mpc})^3$  where we can study haloes with masses ranging from  $10^{13}$  up to  $10^{15} h^{-1}M_{\odot}$ . These simulations will be used to analyse both the mass function and the bias of dark-matter haloes. On the other hand, the third series includes simulations covering a volume of  $(150 h^{-1}\text{Mpc})^3$ . They will be used to study the mass function and the bias of low-mass haloes with  $10^{10} < M < 10^{13} h^{-1}M_{\odot}$ .

### 2.2 A note on the definition of $f_{\text{NL}}$

The definition of  $f_{\text{NL}}$  given in equation (1) depends on the cosmic epoch at which it is applied. The reason for this time dependence is that both potentials  $\Phi$  and  $\phi$  grow with time proportionally to  $g(a) = D(a)/a$  with  $D(a)$  the linear growth factor of density fluctuations and  $a$  the Robertson-Walker scale factor.

In this paper, we define  $f_{\text{NL}}$  by applying equation (1) at early times, namely at  $z = \infty$ . Other authors have adopted different conventions. Grossi et al. (2007) use the linearly-extrapolated fields at  $z = 0$  to define  $f_{\text{NL}}$ . Therefore, their values of the  $f_{\text{NL}}$  parameter need to be divided by the factor  $g(\infty)/g(0)$  to match ours. In the WMAP5 cosmology,  $g(\infty)/g(0) \simeq 1.3064$ . On the other hand, Dalal et al. (2008) apply equation (1) at  $z_{\text{start}}$ , the redshift at which they generate the initial conditions for the simulations. This agrees with our definition to better than 0.01 per cent.

The sign convention for the non-linearity parameter might possibly generate further ambiguity. In our simulations, positive values  $f_{\text{NL}}$  correspond to positive skewness of the mass-density probability distribution function. The same convention has been adopted by Grossi et al. (2007), Kang et al. (2007) and Dalal et al. (2008).

**Table 2.** Assumed cosmological parameters.

Name	$h$	$\sigma_8$	$n_s$	$\Omega_m$	$\Omega_b$	$\Omega_\Lambda$
WMAP3	0.73	0.76	0.95	0.24	0.042	0.76
WMAP5	0.701	0.817	0.96	0.279	0.0462	0.721

### 3 THE HALO MASS FUNCTION

One of the long standing efforts in cosmology is to determine the mass function of dark matter haloes  $n(M, z)$  – i.e. the number of haloes per unit volume per unit mass at redshift  $z$  – from the statistical properties of the linear density field. Analytical work has suggested that, when expressed in terms of suitable variables, the functional form of  $n(M, z)$  should be universal to changes in redshift and cosmology (Press & Schechter 1974; Bond et al. 1991; Sheth & Tormen 1999). N-body simulations have shown that this is approximately true when structure formation is seeded by Gaussian perturbations (Jenkins et al. 2001; Evrard et al. 2002; White 2002; Warren et al. 2006; Tinker et al. 2008).

Following these studies, we describe the halo abundance in our simulations through the following functional form

$$\frac{dn(M, z)}{dM} = f(\sigma) \frac{\bar{\rho}_m}{M} \frac{d \ln[\sigma^{-1}(M, z)]}{dM}. \quad (2)$$

where  $\bar{\rho}_m$  is the mean background matter density today, and  $\sigma(M, z)$  is the variance of the linear density field

$$\sigma^2(M, z) = \frac{1}{2\pi^2} \int_0^\infty k^2 P(k, z) W^2(k, M) dk, \quad (3)$$

with  $W^2(k, M)$  some window function with mass resolution  $M$  (here top-hat in real space). The validity of equation (2) has been widely tested against numerical simulations and useful parameterisations for  $f(\sigma)$  have been provided starting from Gaussian initial conditions (Sheth & Tormen 1999; Jenkins et al. 2001; Warren et al. 2006). These fitting functions have an accuracy ranging from 5 to 20 per cent depending on redshift, cosmology, and the exact definition of halo masses. Recently, Tinker et al. (2008) have detected deviations from universality in  $f(\sigma)$ : redshift-dependent corrections are needed to match the mass function in simulations with an accuracy of 5 per cent. This result is however based on haloes identified with the spherical overdensity algorithm. It is well known that the mass function of FOF haloes shows a more universal scaling even though other halo finders might be more directly linked to actual observables (Jenkins et al. 2001; Tinker et al. 2008). One should anyway keep in mind that baryonic physics can cause 30 per cent deviations in  $n(M, z)$  with respect to the pure dark-matter case (Stanek et al. 2008).

#### 3.1 Halo mass function from Gaussian initial conditions

The halo mass functions extracted from our Gaussian simulations – Run 1.0 (triangles), Run 2.0 (squares), and Run 3.0 (circles) – are presented in Figure 1. The combination of different box sizes allows us to cover the very wide range  $-1.2 < \ln \sigma^{-1} < 1.1$  which roughly corresponds to the mass interval  $2 \times 10^{10} < M < 5 \times 10^{15} h^{-1} M_\odot$  at  $z = 0$ . Note that, at a fixed redshift, larger values of  $\sigma^{-1}$  correspond to

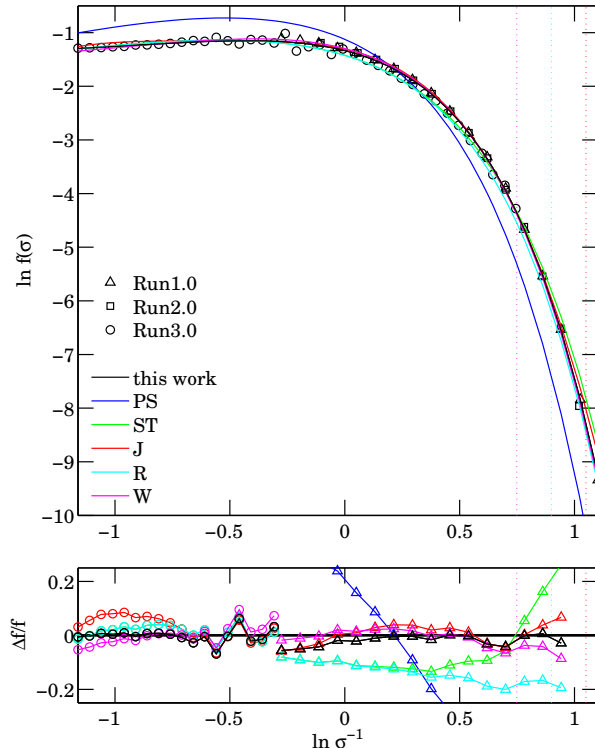


**Figure 1.** The universal mass function in our Gaussian simulations Run 1.0 (triangles), Run 2.0 (squares), and Run 3.0 (circles) is compared with a number of fitting formulae listed in Table 3. Data are equispaced in  $\ln \sigma^{-1}$  and only bins containing more than 30 haloes are shown. The vertical dotted lines indicate the upper mass limits used in Jenkins et al. (2001), Reed et al. (2003), and Warren et al. (2006). The corresponding low-mass limits are all equal or smaller than  $\ln \sigma^{-1} = -1.2$ . The lower panel shows the residuals  $\frac{\Delta f}{f} = \frac{(\text{fit} - \text{data})}{\text{data}}$  between our data points and the different fitting functions. Here we only show data with a better accuracy than 5 per cent. For clarity only outputs from Run 1.0 (triangles,  $\ln \sigma^{-1} > -0.4$ ) and Run 3.0 (circles,  $\ln \sigma^{-1} < -0.4$ ) are plotted.

higher masses. On the other hand, with increasing the redshift, larger values of  $\sigma^{-1}$  are associated with a given halo mass. Even though datapoints correspond to different redshifts and cosmologies, they all form a well defined sequence. This indicates that the function  $f(\sigma)$  is universal to great accuracy. A number of fitting formulae have been proposed in the literature to parameterise this sequence. In Figure 1, we compare some of them (summarised in Table 3) with our datapoints. Fractional deviations between models and data are shown in the bottom panel. Barring the classical Press-Schechter result, all the fitting formulae describe our data to better than 20 per cent. The best agreement is found all over the mass range with Warren et al. (2006) followed by Jenkins et al. (2001) which both show deviations from our data at the 10 per cent level. The Sheth & Tormen (1999) model also provides an accurate description of the data for  $\ln \sigma^{-1} > 0.75$  but tends to overestimate the abundance of the most massive objects. On the other hand, the fit by Reed et al. (2003) tends to underestimate the high-mass tail of the mass function. Overall our findings are in good agreement with Heitmann et al. (2006) and Lukić et al. (2007).



**Table 3.** Widely used parameterisations for the halo mass function deriving from Gaussian initial conditions.

Acronym	Reference	Functional form	Parameters
PS	Press & Schechter (1974)	$f_{\text{PS}}(\sigma) = \sqrt{\frac{2}{\pi}} \frac{\delta_c}{\sigma} \exp\left(-\frac{\delta_c^2}{2\sigma^2}\right)$	$\delta_c = 1.686$
ST	Sheth & Tormen (1999)	$f_{\text{ST}}(\sigma) = A \sqrt{\frac{2a}{\pi}} \frac{\delta_c}{\sigma} \exp\left(-\frac{a \delta_c^2}{2\sigma^2}\right) \left[1 + \left(\frac{\sigma^2}{a \delta_c^2}\right)^p\right]$	$A = 0.322, a = 0.707, p = 0.3$
J	Jenkins et al. (2001)	$f_{\text{J}}(\sigma) = A \exp(- \ln \sigma^{-1} + B P)$	$A = 0.315, B = 0.61, p = 3.8$
R	Reed et al. (2003)	$f_{\text{R}}(\sigma) = f_{\text{ST}}(\sigma) \exp\left(\frac{-a}{\sigma(\cosh 2\sigma)^b}\right)$	$a = 0.7, b = 5$
W	Warren et al. (2006)	$f_{\text{W}}(\sigma) = A(\sigma^{-a} + b) \exp\left(-\frac{c}{\sigma^2}\right)$	$A=0.7234, a=1.625, b=0.2538, c=1.1982$
T	Tinker et al. (2008)	$f_{\text{T}}(\sigma) = A \left[\left(\frac{\sigma}{b}\right)^{-a} + 1\right] \exp\left(-\frac{c}{\sigma^2}\right)$	vary with halo overdensity

Following Warren et al. (2006) and Tinker et al. (2008), we fit the outcome of the simulations with the function

$$f(\sigma) = \left[D + B \left(\frac{1}{\sigma}\right)^A\right] \exp\left(-\frac{C}{\sigma^2}\right). \quad (4)$$

The best-fitting parameters have been determined through  $\chi^2$  minimisation using the Markov Chain Monte Carlo method, and read:

$$\begin{aligned} A &= 1.797 \pm 0.018 \\ B &= 0.6441 \pm 0.0029 \\ C &= 1.1974 \pm 0.0045 \\ D &= 0.2280 \pm 0.0023. \end{aligned} \quad (5)$$

In terms of the parameterisation given in Warren et al. (2006) and reported in Table 3, this corresponds to  $(A, a, b, c) = (0.6441, 1.797, 0.3542, 1.1974)$ . The fit in equation (5) describes our dataset up to deviations of a few per cent over the entire mass and redshift ranges for Run 1.0 and Run 2.0, while it shows slightly larger deviations (up to nearly 10 per cent) towards the high-mass end of Run 3.0 (see Figure 1). It is important to remember, however, that Run 3.0 covers a much smaller volume than the others and thus is more severely affected by sample variance.

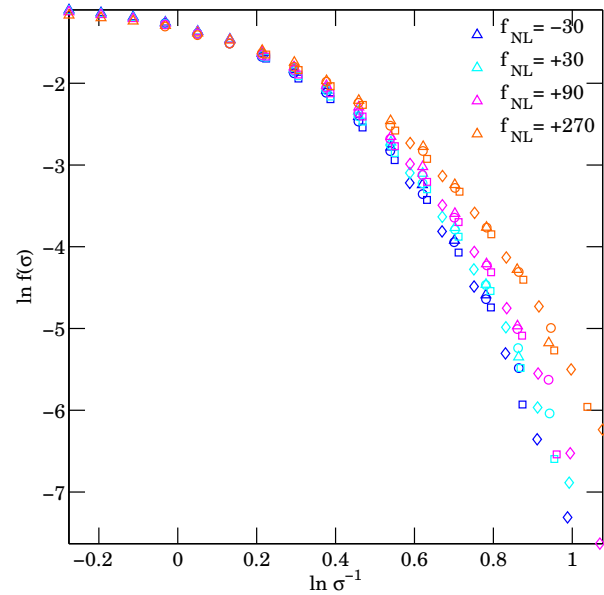
### 3.2 The universal mass function from primordial non-Gaussianity

Is the function  $f(\sigma^{-1})$  universal also in the non-Gaussian case? This question is addressed in Figure 2 where we combine the output of our main series of simulations at four redshifts ( $z = 0, 0.5, 1, 2$ ) to test the scaling of the mass function in terms of  $\sigma^{-1}$ . Only bins containing at least 20 haloes are considered. Within a certain tolerance, the halo mass functions at different masses and redshifts all lie on the same curve for a given  $f_{\text{NL}}$ .

We thus generalise equation (2) to non-Gaussian initial conditions by assuming that

$$\frac{dn(f_{\text{NL}}, M, z)}{dM} = f(f_{\text{NL}}, \sigma) \frac{\bar{\rho}_m}{M} \frac{d \ln[\sigma^{-1}(M, z)]}{dM}, \quad (6)$$

and we provide a fitting formula for  $f(f_{\text{NL}}, \sigma)$ . Given the similarity to the Gaussian case, we still adopt the functional form given in Equation (4) but let the parameters  $A, B, C, D$  vary with  $f_{\text{NL}}$ . The best-fitting values have been determined in two steps. We first used a Markov Chain Monte Carlo method to determine  $A, B, C, D$  at fixed  $f_{\text{NL}}$  through  $\chi^2$  minimisation. The results suggest that the  $f_{\text{NL}}$  dependence

**Figure 2.** Universality of the mass function arising from non-Gaussian initial conditions. Colors refer to simulations with different values of  $f_{\text{NL}}$  as indicated by the labels. Symbols identify the redshift of the simulation output from which the mass function has been calculated, namely  $z = 0$  (triangles),  $0.5$  (circles),  $1$  (squares),  $2$  (diamonds).

Parameter	P1	P2
A	2.007	-0.0054
B	0.558	-0.0012
C	1.206	-0.0021
D	0.343	-0.0006

**Table 4.** Best-fitting values for the linear coefficients of the mass-function parameters given in equation (7). The quoted values are truncated at the first digit which is affected by the statistical errors. This provides an accurate description of our simulations for  $-30 \leq f_{\text{NL}} \leq 90$ .

for each parameter of the mass function can be accurately described by polynomials of different orders. Eventually, we used the data to derive the coefficients of these polynomials.

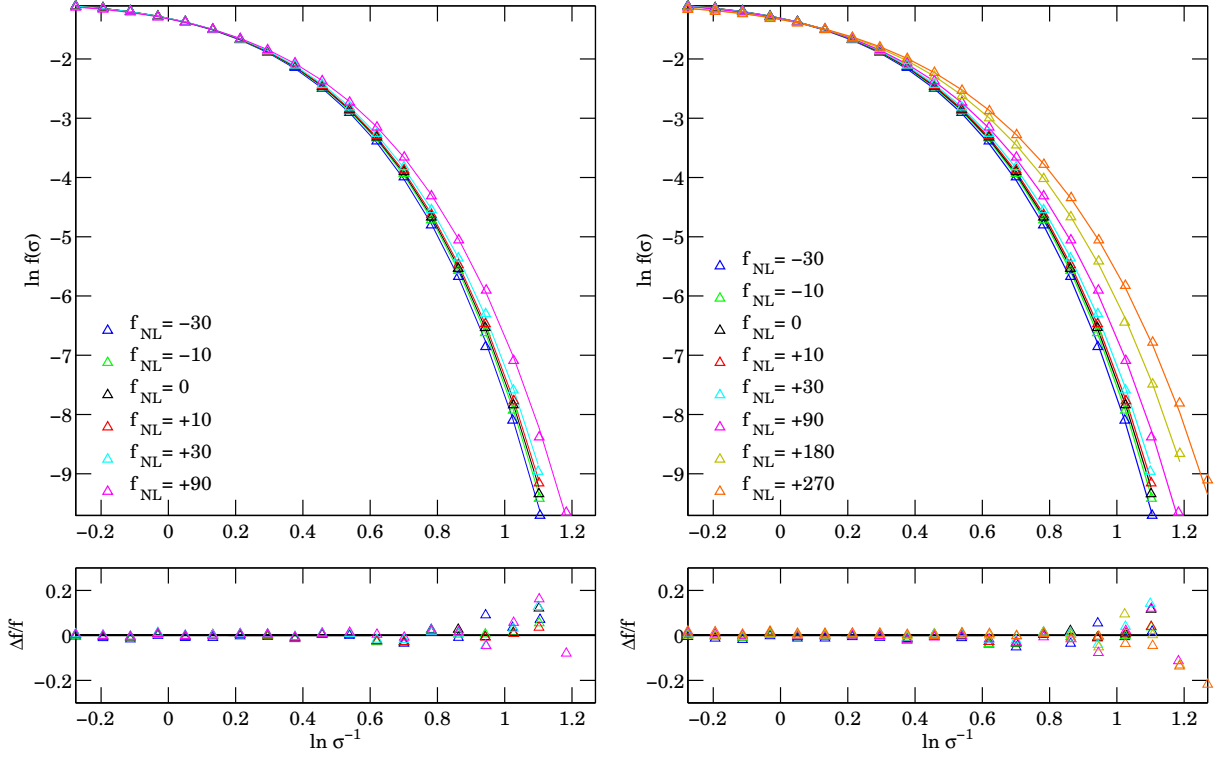


**Figure 3.** Comparison between the halo mass function from our main series of simulations (triangles) and the corresponding fitting functions (lines). Values  $-30 \leq f_{\text{NL}} \leq 90$  and the fit in equation (7) are considered in the left panel. All the simulations and the polynomial fit in equations (8) and (9) are shown in the right panel.

Parameter	p1	p2	p3	p4	p5
A	1.998	-5.8e-3	-2.7e-6	0	0
B	0.555	-1.4e-3	3.8e-6	-3.0e-8	2.2e-10
C	1.205	-2.3e-3	2.0e-6	0	0
D	0.344	-5.6e-4	2.6e-6	4.0e-8	-2.4e-10

**Table 5.** As in Table 4 but for the fitting formula in equations (8) and (9). This accurately describes the mass function in all our non-Gaussian simulations ( $-30 \leq f_{\text{NL}} \leq 270$ ).

The degree of complexity required to fit the simulation data grows considerably with increasing  $f_{\text{NL}}$ . For relatively small amounts of primordial non-Gaussianity, characterised by  $-30 \leq f_{\text{NL}} \leq 90$ , the mass-function parameters in equation (4) are well approximated by the linear relation

$$P(f_{\text{NL}}) = p_1 + p_2 \cdot f_{\text{NL}}, \quad \text{for } P = A, B, C, D. \quad (7)$$

Table 4 lists the corresponding best-fitting parameters. The quality of this fitting formula is assessed in the left panel of Figure 3, where the mass function for the simulations with  $f_{\text{NL}} = -30, -10, 0, +10, +30, +90$  is compared with the corresponding fit. Residuals (shown in the bottom panel) are much smaller than 5 per cent over the range  $0.78 < \sigma^{-1} < 3.07$  corresponding to the mass interval  $1.6 \times 10^{13} < M < 5.4 \times 10^{15} h^{-1} M_{\odot}$  at  $z = 0$ . On the other hand, equation (7) is not suitable to account for values of  $f_{\text{NL}}$  substantially larger than 90. To obtain an accurate fit of the halo mass function over the range  $-30 \leq f_{\text{NL}} \leq 270$  we had to consider

polynomials up to 4<sup>th</sup> order in  $f_{\text{NL}}$ :

$$P(f_{\text{NL}}) = p_1 + p_2 \cdot f_{\text{NL}} + p_3 \cdot f_{\text{NL}}^2, \quad \text{for } P = A, C \quad (8)$$

and

$$P(f_{\text{NL}}) = p_1 + p_2 \cdot f_{\text{NL}} + p_3 \cdot f_{\text{NL}}^2 + p_4 \cdot f_{\text{NL}}^3 + p_5 \cdot f_{\text{NL}}^4, \quad (9) \\ \text{for } P = B, D.$$

The best-fitting values of the parameters above are listed in Table 5 while the corresponding functions are compared with the simulation data in the left panel of Figure 3. Also in this case residuals are substantially smaller than 5 per cent for  $\sigma^{-1} < 3.07$ .

The universality of the fitting formula in equation (6) has been further tested against our non-Gaussian simulation of the WMAP3 cosmology, Run 2.270, which has not been used to determine the best-fitting parameters. This blind check shows that, in the range  $-0.27 < \ln \sigma^{-1} < 0.94$  (roughly corresponding to  $1.6 \times 10^{13} < M < 2.2 \times 10^{15} h^{-1} M_{\odot}$  at  $z = 0$ ), the provided fit reproduces the mass function with an accuracy of 5 per cent, although it underestimates the very-high-mass tail by nearly 20 per cent.

We warn the readers against extending our fitting formulae beyond their range of validity, in particular at low halo masses. The simulations of our main series resolve  $10^{13} h^{-1} M_{\odot}$  haloes with 100 particles. For  $f_{\text{NL}} \neq 0$ , our analytical formulae for the mass function have been derived using only haloes that are more massive than this limit. Since the high-mass tail of the mass function is enhanced (suppressed) for positive (negative) values of  $f_{\text{NL}}$  with respect to the Gaussian case, mass conservation requires that

the opposite effect is seen at lower masses. We have directly tested this using Run 3.90 (which has a boxsize 8 times smaller than for the simulations in the main series but the same number of particles) and indeed found that the fitting formulae in equations (8) and (9) systematically overestimate the abundance of small mass haloes by 10-30 per cent. We will address the low-mass tail of the mass function for  $f_{\text{NL}} \neq 0$  in future work.

On the other hand, for Gaussian initial conditions, we combined simulations with different box sizes to derive the fitting function in equations (4) and (5). This allowed us to extend the validity of our fit to the much wider mass range  $2.4 \times 10^{10} < M < 5 \times 10^{15} h^{-1} M_{\odot}$ .

Our fitting formulae give three different approximations for the universal mass function in the Gaussian case. It is worth stressing that the fit given in equations (4) and (5) has to be preferred as it has been obtained from a richer dataset spanning a much wider range of halo masses. Note, however, that in the overlapping mass range (i.e. for masses above  $10^{13} h^{-1} M_{\odot}$  at  $z = 0$ ), our different fitting functions never deviate by more than 3-4 per cent. Also note that our two fitting functions for the non-Gaussian simulations agree by better than 1 per cent for  $-10 \leq f_{\text{NL}} \leq 30$  and by a few per cent for  $f_{\text{NL}} = -30$  and  $f_{\text{NL}} = +90$ .

#### 4 MATTER POWER SPECTRUM

In this section we study how non-Gaussian initial conditions influence the power spectrum of the mass density field. At tree level, the power spectrum does not depend on  $f_{\text{NL}}$  in Eulerian perturbation theory. However, one-loop corrections make the power spectrum  $f_{\text{NL}}$ -dependent. Qualitatively, theoretical expectations are that positive (negative) values of  $f_{\text{NL}}$  tend to enhance (suppress) the amplitude of the power spectrum on non-linear scales. In Figure 4 we plot the ratio of power spectra  $P(k, f_{\text{NL}})/P(k, f_{\text{NL}} = 0)$  extracted from the simulations of our main series at redshifts  $z = 0$  and 1. The matter power spectrum of non-Gaussian models appears to deviate already by a few per cent at  $k = 0.1 h \text{ Mpc}^{-1}$ . As expected, deviations become more severe with increasing the wavenumber  $k$ . Our results are in good agreement with the perturbative calculations by Taruya et al. (2008). We note, however, that Grossi et al. (2008) found smaller deviations between the non-Gaussian and Gaussian power spectra at larger values of  $k$  and  $f_{\text{NL}}$ .

Our results have two important practical implications. First, the widespread habit of using the Gaussian matter power spectrum to determine non-Gaussian bias parameters leads to scale-dependent systematic errors that might become severe when high-precision is required. Second, primordial non-Gaussianity modifies the power-spectrum on the scales where baryonic oscillations (BAOs) are present. Reversing the argument, the BAOs impressed in the two-point statistics could be also used to constrain the value of  $f_{\text{NL}}$ . Note however, that all probes based on galaxy clustering will suffer from uncertainties in the bias parameter (and its scale dependence) that might hinder a measure of  $f_{\text{NL}}$  based on the study of BAOs. On the other hand, weak lensing studies will directly measure the matter power spectrum and the question is whether one can distinguish the effect of

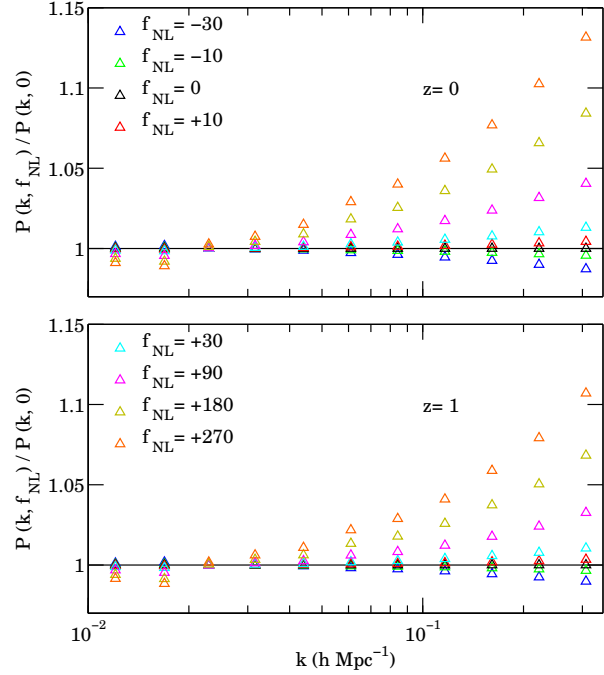


**Figure 4.** Ratio between the matter power spectra of non-Gaussian and Gaussian simulations at redshift  $z = 1$  (bottom) and  $z = 0$  (top). Data are extracted from the N-body simulations in our main series where identical random phases have been used to generate  $\phi$  for all values of  $f_{\text{NL}}$ .

$f_{\text{NL}}$  with respect to those of other cosmological parameters (especially  $\sigma_8$ ). We will get back to this in future work.

#### 5 HALO CLUSTERING

The clustering of dark-matter haloes is biased relative to that of the underlying mass distribution by an amount which depends on halo mass, redshift, and the scale at which the clustering is considered (see e.g. Mo & White 1996; Catelan et al. 1998; Smith et al. 2007). For Gaussian initial conditions, this has been widely tested against numerical simulations (e.g. Sheth et al. 2001; Seljak & Warren 2004; Tinker et al. 2005).

In general, the halo bias can be quantified using either the power spectrum of the halo density field,  $P_{\text{hh}}$ , or the cross-spectrum between the halo and the underlying matter density field,  $P_{\text{hm}}$ . In the two cases the bias reads

$$b_{\text{hh}}(k, M, z) = \sqrt{\frac{P_{\text{hh}}(k, M, z)}{P(k, z)}}, \quad (10)$$

or

$$b_{\text{hm}}(k, M, z) = \frac{P_{\text{hm}}(k, M, z)}{P(k, z)}, \quad (11)$$

where  $P(k, z)$  is the matter power spectrum. If the bias due to halo formation is local and deterministic then  $b_{\text{hh}} = b_{\text{hm}}$  apart from measurement errors. However, in the presence of a stochastic component that does not correlate with the density field  $b_{\text{hh}} \geq b_{\text{hm}}$ . In practice, however, the measurement of all power spectra is affected to some level by shot noise due

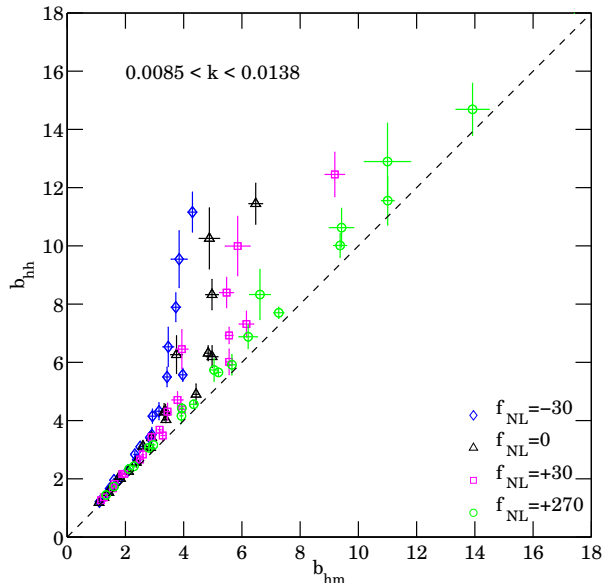


**Figure 5.** The halo bias from the halo-halo power spectrum (with no discreteness corrections) is plotted against the halo bias from the halo-matter cross spectrum. Whenever the density of haloes is high enough, the two estimates are very close showing that little stochasticity between mass and halo overdensities is present on the scales of interest (indicated in  $h \text{ Mpc}^{-1}$  in the label). The excess in  $b_{hh}$  for rare, massive haloes is likely due to shot noise. Note that large positive values of  $f_{NL}$  correspond to more massive haloes and thus allow more accurate measures of high bias parameters.

to the discrete nature of dark-matter haloes and N-body particles. If the distribution of the tracers can be approximated as the Poisson sampling of an ideal density field, then the measured power spectrum corresponds to that of the underlying field plus the mean volume per particle (Peebles 1980). Discreteness effects are thus expected to be negligible for  $P$  and  $P_{hm}$  due to the large number density of particles in the simulations. On the other hand, massive haloes are rare and, being extended objects, cannot be modelled as the Poisson sampling of a continuous distribution (Mo & White 1996, Magliocchetti & Porciani 2003, Porciani in preparation). It is not clear then how to correct for the discreteness effect in their power spectrum (Smith et al. 2007). For these reasons we use  $b_{hm}$  in our analysis and we adopt  $b_{hh}$  (without performing any discreteness correction) just to cross-check the results (see Figure 5).

### 5.1 Halo bias from Gaussian initial conditions

It is well known that the halo bias factor from Gaussian initial conditions is approximately scale-independent for small values of the wavenumber  $k$ . We will refer to this asymptotic value on large scales as the “linear bias” and denote it by  $b_0$ . Similarly to the halo mass function, when expressed in terms of  $\sigma^{-1}$ , the linear bias assumes a universal form which, within a given accuracy, is independent of redshift and just weakly dependent on cosmology (e.g. Sheth & Tormen 1999; Seljak & Warren 2004).

We measure the linear bias for the haloes in our simulations as follows. We first determine the functions  $b_{hh}$  and

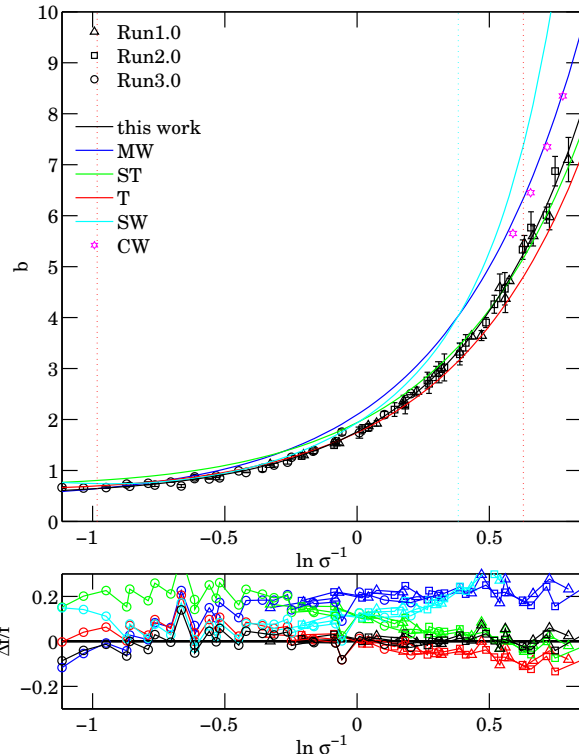


**Figure 6.** Linear halo bias from the Gaussian simulations Run 1.0 (triangles), Run 2.0 (squares), and Run 3.0 (circles), as a function of  $\sigma^{-1}$ . Only bins containing more than 1000 haloes are shown. The solid lines correspond to the functions listed in Table 6 as indicated by the labels. The four hexagons correspond to the data at  $z = 10$  by Cohn & White (2008). The vertical dotted lines indicate the maximum and minimum  $\sigma^{-1}$  considered by Tinker et al. (2005) (red) and Seljak & Warren (2004) (cyan, in this case the minimum  $\sigma^{-1}$  coincides with the frame of the figure).

$b_{hm}$  by directly applying equations (10) and (11). Within the statistical uncertainties, both functions approach asymptotically to a constant on large scales ( $k < 0.05 h \text{ Mpc}^{-1}$ ). We use the average of the bias function measured in the range  $0.01 < k < 0.05 h \text{ Mpc}^{-1}$  (4  $k$ -bins) as our estimate of the linear bias. The standard error of the mean is used to quantify the corresponding statistical uncertainty.

In Figure 6 we show the linear bias obtained from Run 1.0 (triangles), Run 2.0 (squares) and Run 3.0 (circles) as a function of  $\sigma^{-1}$ . Simulation data from snapshots between  $z = 0$  and  $z = 2$  are compared with the commonly used parameterisations listed in Table 6. Our results are in good agreement with the fit by Sheth et al. (2001) for large masses and with that by Tinker et al. (2005) for smaller masses. Note that by combining simulation boxes we are able to explore a larger interval of  $\sigma^{-1}$  than previous studies.

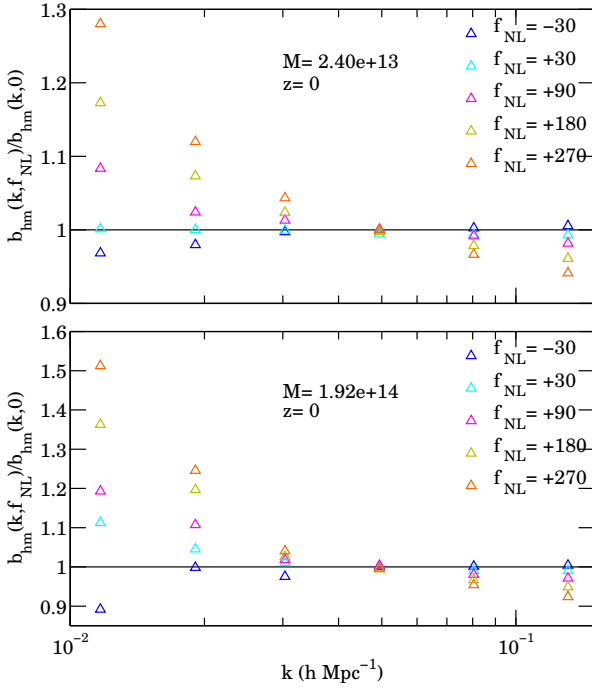
Given that no existing model for the linear bias accurately reproduces our results over the entire mass range spanned by the simulations, we decided to derive a new fitting formula. In particular, we parameterised the outcome of our simulations as

$$b_0 = B_0 + B_1 \sigma^{-1} + B_2 \sigma^{-2}, \quad (12)$$



**Table 6.** Commonly used parameterisations for the linear bias arising from Gaussian initial conditions.

Acronym	Reference	Functional form	Parameters and Variables
MW	Mo & White (1996)	$b_{\text{MW}} = 1 + \frac{\delta_c}{\sigma^2} - \frac{1}{\delta_c}$	$\delta_c \simeq 1.686$
ST	Sheth et al. (2001)	$b_{\text{ST}} = 1 + \frac{1}{\sqrt{a}\delta_c} \left[ \sqrt{a} \left( a \frac{\delta_c^2}{\sigma^2} \right) + \sqrt{ab} \left( a \frac{\delta_c^2}{\sigma^2} \right)^{1-c} - \frac{\left( a \frac{\delta_c^2}{\sigma^2} \right)^c}{\left( a \frac{\delta_c^2}{\sigma^2} \right)^c + b(1-c)(1-c/2)} \right]$	$\delta_c = 1.686$ $a = 0.707, b = 0.5, c = 0.6$
SW	Seljak & Warren (2004)	$b_{\text{SW}} = 0.53 + 0.39(x^{0.45}) + \frac{0.13}{(40x+1)} + 5 \times 10^{-4}x^{1.5}$	$x = \frac{M}{M_\star}$
T	Tinker et al. (2005)	$b_{\text{T}} = b_{\text{ST}}$	$\delta_c = 1.686, a = 0.707, b = 0.35, c = 0.80$

**Figure 7.** Scale-dependent halo bias arising from non-Gaussian initial conditions. Results are shown in terms of the ratio between the bias functions measured from a simulation with a given  $f_{\text{NL}}$  and with  $f_{\text{NL}} = 0$  at fixed halo mass (indicated by the label in units of  $h^{-1}M_\odot$ ). Note that in the Gaussian case the bias keeps nearly constant for  $k < 0.05 h \text{ Mpc}^{-1}$ .

and used  $\chi^2$  minimisation to find

$$\begin{aligned} B_0 &= 0.531 \pm 0.014 \\ B_1 &= -0.249 \pm 0.039 \\ B_2 &= 1.474 \pm 0.025 \end{aligned} \quad (13)$$

This fit (which reproduces the numerical data with great accuracy in the range  $-1.1 < \ln \sigma^{-1} < 0.8$ ) should be considered as the linear bias naturally associated with the mass function given in equations (4) and (5).

## 5.2 Halo bias from non-Gaussian initial conditions

Recent analytical models, have suggested that the halo bias arising from non-Gaussian initial conditions of the local type does not tend to a constant on large scales. Rather, the deviation from the Gaussian case should follow

$$\begin{aligned} \Delta b &= b(k, M, z, f_{\text{NL}}) - b(k, M, z, f_{\text{NL}} = 0) = \\ &= 3 f_{\text{NL}} [b_0(M, z) - 1] \frac{\delta_c}{D(z)} \frac{H_0^2}{c^2} \frac{\Omega_m}{k^2 T(k)}, \end{aligned} \quad (14)$$

where  $\delta_c = 1.686$ ,  $c/H_0 = 2997.9 h^{-1} \text{ Mpc}$  is the Hubble radius,  $T(k)$  is the matter transfer function, and  $D(z)$  is the linear growth factor of matter perturbations normalised to unity at  $z = 0$  (Dalal et al. 2008; Matarrese & Verde 2008; Slosar et al. 2008; Afshordi & Tolley 2008; McDonald 2008). The numerical simulations by Dalal et al. (2008) have indeed shown that the halo bias is scale dependent even for small values of  $k$  in non-Gaussian cosmologies (with  $|f_{\text{NL}}| = 100, 500$ ) and found qualitative agreement with equation (14). In Figure 7, we show how the bias depends on scale in our simulations which also consider smaller values of  $|f_{\text{NL}}|$ . Our results confirm the presence of a strongly scale-dependent bias. Larger values of  $|f_{\text{NL}}|$  correspond to a more marked scale dependence. Note, however, that for  $k > 0.05 h \text{ Mpc}^{-1}$  the non-Gaussian deviation  $\Delta b$  changes sign. This result implies that equation (14) can only hold asymptotically on very large scales.

To proceed with a detailed analysis of our simulations, we find it convenient to rewrite equation (14) as

$$\Delta b = f_{\text{NL}} (b_0 - 1) \frac{\Gamma}{\alpha(k, z)}, \quad (15)$$

where  $\Gamma = 3 \delta_c \Omega_m H_0^2 / c^2$  and  $\alpha(k, z) = k^2 T(k) D(z)$ . In Figure 8 we test the scaling of  $\Delta b$  with redshift, linear bias and wavenumber for  $f_{\text{NL}} = 270$  (where we have the best signal-to-noise ratio at high halo mass). Similar results are obtained with different values of  $f_{\text{NL}}$ . The quantity shown is  $\Delta b \alpha / \Gamma$  which should correspond to  $f_{\text{NL}} (b_0 - 1)$  if the analytical model provides a good description of the data. This quantity is indicated by a dashed line. The following two trends clearly emerge from the data. For small values of  $k$ , the model underestimates the data by a factor of a few independently of  $b_0$  and  $z$ . On smaller scales, discrepancies become less and less severe until  $k \sim 0.04 h \text{ Mpc}^{-1}$  where the model starts to overestimate the data systemati-

cally. The  $k$ -dependence of  $\Delta b$  is therefore different than in equation (14).

The data also drop a hint that, for  $k > 0.01 h \text{ Mpc}^{-1}$ , the scaling with  $b_0 - 1$  might only persists up to a maximum value of  $b_0, b_{0,\text{max}}$ . For  $b_0 > b_{0,\text{max}}$  it appears that the values of  $\Delta b$  are always smaller than expected from the extrapolation of the trend  $b_0 - 1$  determined at smaller  $b_0$ . The value of  $b_{0,\text{max}}$  seems to depend both on redshift and wavenumber and roughly corresponds to constant halo mass for a given  $k$ . However, uncertainties in  $\Delta b$  at these high masses become very large and it is difficult to judge how robust the existence of  $b_{0,\text{max}}$  really is. We note anyway that when we tried to fit data at different redshifts (for a given  $f_{\text{NL}}$  and  $k > 0.015 h \text{ Mpc}^{-1}$ ) by adding a variable normalisation constant in front of equation (14), we systematically obtained significantly different fits (at a confidence level of  $2.5 \sigma$ ) at different redshifts. This trend disappears when only the lowest values of  $b_0$  are considered at each redshift for the fit.

Data from simulations with all the considered values of  $f_{\text{NL}}$  are shown with different symbols and colors in Figure 9. Each panel refers to a particular wavenumber bin (indicated by the label). The model in equation (14) is again indicated by a dashed line. Note that, in most cases, it substantially deviates from the simulation data. In particular,  $\Delta b$  measured from the simulations shows a much stronger  $k$ -dependence than the analytical formula, as already seen in Figure 8. In general, the overall amplitude of  $\Delta b$  drops by an extra factor of  $\sim 3$  with respect to  $k^2 T(k)$  when moving from  $k \sim 0.01 h \text{ Mpc}^{-1}$  to  $k \sim 0.05 h \text{ Mpc}^{-1}$  independently of  $b_0$  and  $f_{\text{NL}}$ . Also,  $\Delta b$  does not seem to scale linearly with  $f_{\text{NL}}$  while its linear dependence on  $b_0 - 1$  appears to be solid, at least for  $b_0 < b_{0,\text{max}}$ . We thus introduce a correcting factor  $\beta(f_{\text{NL}}, k)$  defined by

$$\Delta b = \beta(f_{\text{NL}}, k) f_{\text{NL}} (b_0 - 1) \frac{\Gamma}{\alpha(k, z)} \quad (16)$$

and we measure it by fitting the simulation data for  $b(k, M, z, f_{\text{NL}})$  and  $b(k, M, z, 0)$  at constant values of  $f_{\text{NL}}$  and  $k$ . We use an effective variance weighted least squares method to simultaneously account for errorbars on both bias parameters. The best-fitting values are reported in Table 7 and can be used to compute the function  $\beta$  by interpolation. The final expression for  $\Delta b$ , corrected with the  $\beta$  factor, is shown in Figure 9 with solid lines.

Data in Table 7 have an amazing regularity. Apart from a normalisation constant, each column (row) shows the same linear trend with  $k$  ( $f_{\text{NL}}$ ). This suggests that, within the explored parameter range ( $0.01 < k < 0.05 h \text{ Mpc}^{-1}$  and  $-30 \leq f_{\text{NL}} \leq 270$ ),

$$\beta(k, f_{\text{NL}}) = \beta_0 (1 - \beta_1 f_{\text{NL}}) (1 - \beta_2 k) . \quad (17)$$

We thus use this equation to fit the original data for  $b$  and  $b_0$  and find

$$\begin{aligned} \beta_0 &= 3.32 \pm 0.10 , \\ \beta_1 &= (1.17 \pm 0.12) \times 10^{-3} , \\ \beta_2 &= 14.9 \pm 0.7 h^{-1} \text{ Mpc} , \end{aligned} \quad (18)$$

at the 68.3 per cent confidence level. Note that we computed

the power spectra in finite-sized bins of the wavenumber, so that there is some degree of ambiguity in associating the results with a given value of  $k$ . Unfortunately the choice plays a role in determining  $\beta$  as  $\alpha$  is a steep function of  $k$  on the scales of interest. In Table 7 and in equation (18), we have used the arithmetic mean of the wavenumbers contributing to a given bin. If one instead uses the logarithmic center of the bin,  $\beta_0$  is slightly reduced with a best-fitting value of  $2.89 \pm 0.10$ . The parameters  $\beta_1$  and  $\beta_2$  are unaltered. Therefore, a systematic contribution  $\simeq 0.4$  should be added to the error budget of  $\beta_0$ .

The quadratic dependence of  $\Delta b$  on  $f_{\text{NL}}$  is rather surprising as it cannot be straightforwardly derived from the simple models listed above. It might possibly arise from higher-order terms which have been neglected in the expansion that leads to equation (14). Anyway, it is clearly present in the simulations as it can be seen by looking at the variation of  $\beta$  along a given row in Table 7. Even though the coefficient  $\beta_1$  is small, it already corresponds to a 10 per cent correction for  $f_{\text{NL}} \simeq 85.5$ . Note that a quadratic term breaks the symmetry in the amplitude of  $\Delta b$  between non-linearity parameters with opposite sign and identical absolute value. It is hard to directly test this against our simulations as we just have two runs with  $f_{\text{NL}} < 0$  and both of them correspond to rather small  $|f_{\text{NL}}|$  where the uncertainties in  $\beta$  are large. An alternative explanation for a non-vanishing  $\beta_1$  could be that it artificially derives from imposing a linear relation in  $b_0 - 1$  to data that do not scale linearly for  $b_0 > b_{0,\text{max}}$ . Indeed, just using datapoints with small values of  $b_0$  we derive bigger values of  $\beta$  for large  $f_{\text{NL}}$  (more or less in line with  $\beta_1 = 0$ ). Therefore, what is robust is that at least one of the scalings with  $b_0$  or with  $f_{\text{NL}}$  is incorrect in equation (14). We found that a scaling proportional to  $\gamma_0 (1 + \gamma_1 \log b_0)$  (with  $\gamma_0$  and  $\gamma_1$  two adjustable parameters) does slightly better (in terms of reduced  $\chi^2$ ) than  $\beta_0 (b_0 - 1)$ , at least for  $k > 0.014 h \text{ Mpc}^{-1}$ . However, since the scaling with  $b_0 - 1$  has a sound theoretical basis (Mo & White 1996; Catelan et al. 1998) we preferred to quote our results as in equation (17). From the statistical point of view, the parameters (18) provide an acceptable description of the simulation data to high confidence for all values of  $b_0$ . However, they are particularly accurate for  $b_0 > 2 - 2.5$ , while  $\beta_1 \sim 0$  (with the same  $\beta_0$  and  $\beta_2$ ) has to be preferred for smaller values of  $b_0$ .

The linear correction in  $k$  should be thought of as the first-order term of a series expansion in the wavenumber. We attempted to determine the corresponding quadratic term by considering larger values of  $k$  in the fit (one bin more, up to  $k = 0.0962 h \text{ Mpc}^{-1}$ ). However, values of  $\Delta b$  become small compared with the numerical errors and we found that the quadratic parameter is badly constrained by the data ( $\beta_3 = 34 \pm 34 h^{-2} \text{ Mpc}^2$ ) while the other parameters remain nearly unchanged (and get larger uncertainties). Also note that the Gaussian bias starts to depart from  $b_0$  at  $k > 0.05 h \text{ Mpc}^{-1}$  (see Figure 7) and it is not clear whether equation (14) should still be expected to hold in this regime.

Dalal et al. (2008) derived an expression for  $\Delta b$  which coincides with equation (14) but does not include the linear transfer function. Theoretically, this is hard to understand, as non-Gaussianity is generated well before matter-radiation equality and one should account for the linear evolution of density perturbations. Anyway, due to the different  $k$ -

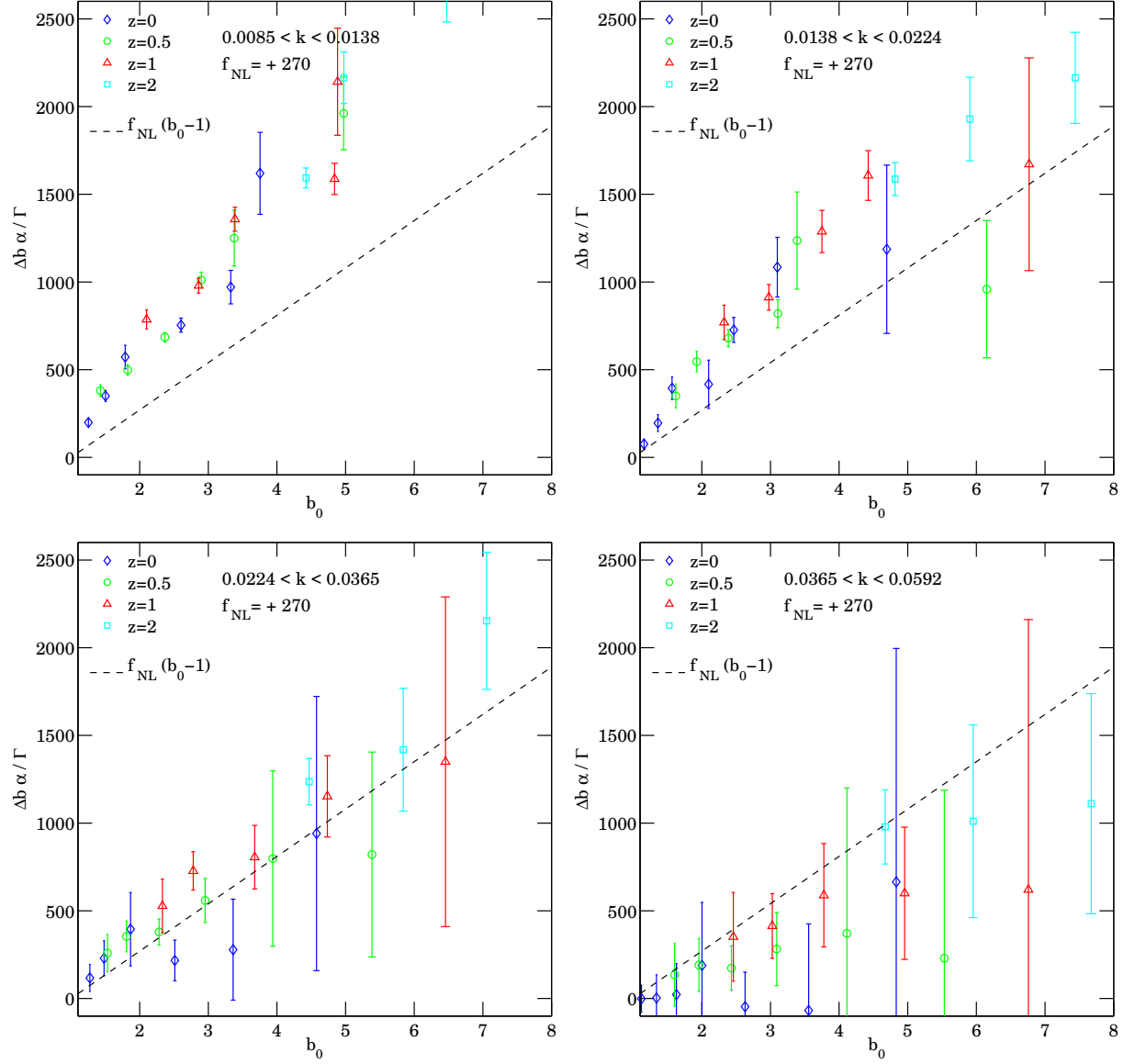


**Figure 8.** The non-Gaussian bias correction  $\Delta b$  as a function of the linear Gaussian bias  $b_0$  for  $f_{\text{NL}} = 270$ . Data from the simulations are indicated by symbols with errorbars and correspond to different redshifts as indicated in the label. The dashed line marks the prediction of the model in equation (14). The wavenumber in the labels is given in units of  $h \text{ Mpc}^{-1}$ . Horizontal errorbars are not drawn to improve readability.

**Table 7.** Best-fitting value and  $1\sigma$  uncertainties for the multiplicative correction  $\beta(k, f_{\text{NL}})$ . The first set of data corresponds to the  $k$ -interval where the Gaussian bias is constant.

$k(h\text{Mpc}^{-1})$	$\beta(k, -30)$	$\beta(k, -10)$	$\beta(k, +10)$	$\beta(k, +30)$	$\beta(k, +90)$	$\beta(k, +180)$	$\beta(k, +270)$
0.0117	$3.11 \pm 0.12$	$2.82 \pm 0.33$	$2.67 \pm 0.36$	$2.68 \pm 0.17$	$2.29 \pm 0.06$	$2.12 \pm 0.04$	$1.92 \pm 0.03$
0.0191	$2.47 \pm 0.30$	$1.51 \pm 0.45$	$2.10 \pm 0.31$	$2.24 \pm 0.48$	$2.03 \pm 0.10$	$1.81 \pm 0.06$	$1.64 \pm 0.05$
0.0303	$2.08 \pm 0.64$	$1.40 \pm 0.64$	$1.77 \pm 0.34$	$1.73 \pm 0.33$	$1.62 \pm 0.20$	$1.36 \pm 0.11$	$1.19 \pm 0.07$
0.0494	$1.00 \pm 0.34$	$1.45 \pm 0.72$	$0.84 \pm 0.43$	$0.80 \pm 0.39$	$0.94 \pm 0.30$	$0.79 \pm 0.15$	$0.64 \pm 0.11$
0.0804	$0.04 \pm 0.99$	$0.86 \pm 0.42$	$1.00 \pm 0.25$	$-0.20 \pm 0.55$	$-0.24 \pm 0.27$	$-0.31 \pm 0.13$	$-0.37 \pm 0.15$

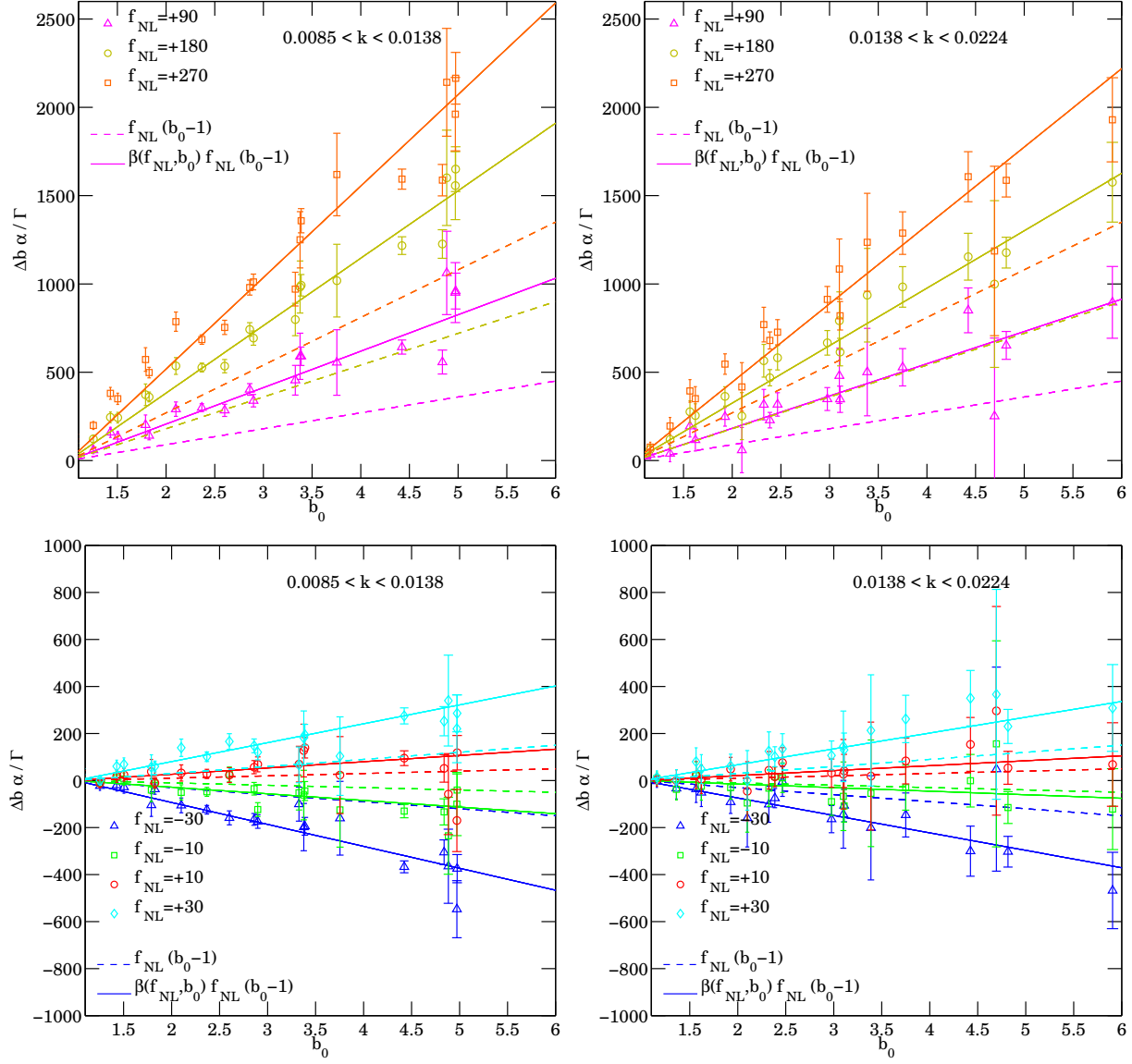


**Figure 9.** As in Figure 8 but for all the simulations of our main series and without distinguishing data from different redshifts. The continuous line corresponds to our best-fitting values of  $\beta$  listed in Table 7.

dependence, their expression for  $\Delta b$  provides a better fit to the simulation data than equation (14) when both models are allowed to vary in amplitude with a tunable free parameter. Note however that, at variance with our equation (17), none of them is able to give an acceptable fit to any interesting confidence level.

## 6 DISCUSSION

Slosar et al. (2008) have used equation (14) to constrain  $f_{\text{NL}}$  by combining measures of the clustering amplitude of luminous red galaxies (LRGs) and quasars from the Sloan Digital Sky Survey. Combining all datasets, they found  $-29 < f_{\text{NL}} < +70$  at 95 per cent confidence. How would this result change based on our simulations? Disentangling the different contributions, the strongest constraints to  $f_{\text{NL}}$

in Slosar et al. (2008) come from the angular power spectrum of quasars with photometric redshifts in the range  $1.45 < z < 2.00$  and a mean bias of  $\sim 2.7$ . Weaker limits are also contributed from the power spectrum of spectroscopic LRGs and the angular spectrum of photometric LRGs. (with a bias of  $\sim 2$  at  $z \sim 0.5$ ). Figure (9) and Table 7 suggest that at the scales of interest ( $0.01 < k < 0.05 h \text{ Mpc}^{-1}$ ) the model given in equation (14) tends to underestimate the scale-dependent bias seen in the simulations. Therefore, a smaller value of  $|f_{\text{NL}}|$  gives a larger  $\Delta b$  than predicted by the analytic model. When applied to the data by Slosar et al. (2008), our correction should thus give tighter limits on  $f_{\text{NL}}$  by a factor between 1 and 3. Because of the strong  $k$ -dependence of the function  $\beta$  it is impossible to give more precise estimates without fitting the power-spectrum data. Note, however, that a larger  $\Delta b$  for a given non-linearity parameter and a steeper  $k$ -dependence, makes determina-

tions of  $f_{\text{NL}}$  even more competitive with respect to studies of CMB anisotropies.

## 7 SUMMARY

We use a series of high-resolution N-body simulations to study the mass function and the clustering properties of dark-matter haloes arising from Gaussian and non-Gaussian initial conditions. In particular, we follow the formation of structure in a universe characterised by the best-fitting parameters from the third- and fifth-year WMAP data releases. We consider non-Gaussianity of the local type and we use 8 different values of  $f_{\text{NL}}$  covering the parameter space currently allowed by studies of the cosmic microwave background, namely  $-30 < f_{\text{NL}} < 270$ . Our main results can be summarised as follows.

(i) The mass function of dark-matter haloes varies with  $f_{\text{NL}}$ . Larger values of the non-linearity parameter correspond to higher abundances of the most massive haloes. We find that, in perfect analogy with the Gaussian case (Jenkins et al. 2001), the halo mass function assumes a universal form. This means that, when expressed in terms of suitable variables, its dependence on redshift and cosmology is erased to very good precision. We parameterise the  $f_{\text{NL}}$ -dependence of the universal mass function and provide an accurate fit for its high-mass end ( $M > 10^{13} h^{-1} M_{\odot}$ ). In the Gaussian case, we extend the fit to a larger interval of halo masses ( $M > 2.4 \times 10^{10} h^{-1} M_{\odot}$ ) by combining simulations with different box sizes. Our fitting function provides a precious tool to forecast constraints on  $f_{\text{NL}}$  from future surveys and to analyze current datasets.

(ii) The matter power-spectrum in non-Gaussian cosmologies departs from the Gaussian one already on very large scales. These scale-dependent deviations can be as high as a few per cent at  $k = 0.06 h^{-1} \text{Mpc}^{-1}$  and, for  $f_{\text{NL}} > 50$ , be well above five per cent at  $k > 0.3 h^{-1} \text{Mpc}^{-1}$ . The discrepancy is systematic: models with positive  $f_{\text{NL}}$  have more large-scale power than the Gaussian case and models with negative  $f_{\text{NL}}$  have less. This warns against the widespread habit of using the Gaussian matter power spectrum to determine non-Gaussian bias parameters when high-precision is required. It also suggests that non-Gaussianity modifies the shape and amplitude of the baryonic-oscillation feature in the two-point statistics.

(iii) We present an accurate fitting formula for the linear bias of dark matter haloes arising from Gaussian initial conditions extending previous work to larger mass intervals. This, together with the mass function fit mentioned above, can be used to constrain parameters of halo-occupation models from clustering data.

(iv) Finally, using both the halo power spectrum and the halo-matter cross spectrum, we confirm the strong  $k$ -dependence of the halo bias on large scales ( $k < 0.05 h \text{Mpc}^{-1}$ ) which was already detected by Dalal et al. (2008). However, we show that commonly used parameterisations based on the peak-background split strongly underestimate the effect on the largest scales and overestimate it at  $k \simeq 0.1 h \text{Mpc}^{-1}$  (where actually it changes sign in the simulations with respect to the models). The analytic model requires corrections which depend on the non-linearity parameter, the wavenumber and, possibly, also on redshift

and clustering strength. We provide a fitting formula which accurately reproduces the outcome of the simulations for  $0.01 < k < 0.05 h \text{Mpc}^{-1}$ . This fit should be employed to constrain  $f_{\text{NL}}$  from future clustering data at low and high redshift.

## ACKNOWLEDGMENTS

All simulations were performed at the Swiss National Supercomputing Center (CSCS) in Manno, Switzerland. AP and OH acknowledge support from the Swiss National Science Foundation. We thank Volker Springel for kindly making the lean version of the GADGET-2 code available to us. We acknowledge discussions with Robert E. Smith and Tommaso Giannantonio. While our paper was being submitted, a related work by Desjacques, Seljak & Iliev (2008) appeared as a preprint.

## REFERENCES

- Afshordi N., Tolley A.J., arXiv:0806.104
- Amara, A., & Refregier, A. 2004, MNRAS, 351, 375
- Bardeen J.M., Bond J.R., Kaiser N., Szalay A.S., 1986, ApJ, 304, 15
- Bartolo N., Komatsu E., Matarrese S., Riotto A., 2004, PhR, 402, 103
- Bartolo N., Matarrese S., Riotto A., 2005, JCAP, 10, 010
- Bertschinger, E. 2001, ApJS, 137, 1
- Bond, J. R., Cole, S., Efstathiou, G., & Kaiser, N. 1991, ApJ, 379, 440
- Buchbinder, E. I., Khoury, J., & Ovrut, B. A. 2008, Physical Review Letters, 100, 171302
- Catelan, P., Lucchin, F., Matarrese, S., & Porciani, C. 1998, MNRAS, 297, 692
- Carbone C., Verde L., Matarrese S., 2008, ApJ, 684, 1
- Cohn J.D., White M., 2008, MNRAS, 385, 2025
- Cooray, A. 2006, Physical Review Letters, 97, 261301
- Creminelli P., Senatore L., 2007, JCAP, 11, 010
- Creminelli P., Senatore L., Zaldarriaga M., 2007, JCAP, 03, 19
- Curto, A., Martinez-Gonzalez, E., Mukherjee, P., Barreiro, R. B., Hansen, F. K., Liguori, M., & Matarrese, S. 2008, arXiv:0807.0231
- Dalal N., Dore' O., Huterer D., Shirokov A., 2008, Phys. Rev. D77, 123514
- Desjacques, V., Seljak, U., & Iliev, I. T. 2008, arXiv:0811.2748
- Evrard, A. E., et al. 2002, ApJ, 573, 7
- Falk T., Rangarajan R., Srednicki M., 1993, ApJ, 403, 1
- Gangui A., Lucchin F., Matarrese S., Mollerach S., 1994, ApJ, 430, 447
- Grinstein, B., & Wise, M. B. 1986, ApJ, 310, 19
- Grossi M., Dolag K., Branchini E., Matarrese S., Moscardini L., 2007, MNRAS, 382, 1261
- Grossi M., Branchini E., Dolag K., Matarrese S., Moscardini L., 2008, arXiv:0805.0276
- Heitmann K., Lukić Z., Habib S., Ricker P.M., 2006, ApJ, 642, 85
- Hikage, C., Matsubara, T., Coles, P., Liguori, M., Hansen, F. K., & Matarrese, S. 2008, MNRAS, 389, 1439



- Jenkins A., 2001, MNRAS, 321, 372
- Jeong, E., & Smoot, G. F. 2007, arXiv:0710.2371
- Jing, Y. P. 1998, ApJ, 503, L9
- Kang X., Norberg P., Silk J., 2007, MNRAS, 376, 343
- Komatsu, E., & Spergel, D. N. 2001, PhRvD, 63, 063002
- Komatsu, E., et al. 2008, arXiv:0803.0547
- Lehners, J.-L., & Steinhardt, P. J. 2008, PhRvD, 77, 063533
- Linde A., Mukhanov V., 1997, PhRvD, 56, 535
- LoVerde M., Miller A., Shandera S., Verde L., 2008, JCAP, 04, 014
- Lucchin, F., Matarrese, S., & Vittorio, N. 1988, ApJl, 330, L21
- Lukić Z., Heitmann K., Habib S., Bashinsky S., Ricker P.M., 2007, ApJ, 671, 1160
- Magliocchetti, M., & Porciani, C. 2003, MNRAS, 346, 186
- Maldacena J., 2003, JHEP, 05, 013
- Matarrese, S., Lucchin, F., & Bonometto, S. A. 1986, ApJ., 310, L21
- Matarrese S., Verde L., Jimenez R., 2000, ApJ, 541, 10
- Matarrese S., Verde L., 2008, ApJ, 677, 77
- McDonald P., arXiv:0806.1061
- Mo, H. J., & White, S. D. M. 1996, MNRAS, 282, 347
- Peebles, P. J. E. 1980, Research supported by the National Science Foundation. Princeton, N.J., Princeton University Press, 1980. 435 p.,
- Pillepich, A., Porciani, C., & Matarrese, S. 2007, ApJ, 662, 1
- Porciani, C., Catelan, P., & Lacey, C. 1999, ApJ, 513, L99
- Press W.H., Schechter P. 1974, ApJ, 187, 425
- Pyne T., Carroll S.M., 1996, PhRvD, 53, 2920
- Reed D., Gardner J., Quinn T., Stadel J., Fardal M., Lake G., Governato F., 2003, MNRAS, 346, 365
- Robinson, J., & Baker, J. E. 2000, MNRAS, 311, 781
- Robinson, J., Gawiser, E., & Silk, J. 2000, ApJ, 532, 1
- Salopek D.S., Bond J.R., 1990, PhRvD, 42, 3936
- Scoccimarro, R., Sefusatti, E., & Zaldarriaga, M. 2004, PhRvD, 69, 103513
- Sefusatti, E., & Komatsu, E. 2007, PhRvD, 76, 083004
- Seljak U., Warren M.S., 2004, MNRAS, 355, 129
- Sheth R.K., Mo H.J., Tormen G., 2001, MNRAS, 323, 1
- Sheth R.K., Tormen G. 1999, MNRAS, 308, 119
- Slosar A., Hirata C., Seljak U., Ho S., Padmanabhan N., 2008, JCAP, 08, 031
- Smith R.E., Scoccimarro R., Sheth R.K. 2007, PhRvD, 75, 3512
- Smith R.E., 2008, arXiv0810.1960S
- Spergel, D. N., et al. 2007, ApJS, 170, 377
- Springel, V. 2005, MNRAS, 364, 1105
- Stanek, R., Rudd, D., & Evrard, A. E. 2008, arXiv:0809.2805
- Taruya A., Koyama K., Matsubara T., 2008, arXiv:0808.4085
- Tinker J.L., Weinberg D.H., Zheng Z., Zehavi I., 2005, ApJ, 631, 41
- Tinker J.L., Kravtsov A.V., Klypin A., Abazajian K., Warren M.S., Yepes G., Gottlober S., Holz D.E., 2008, arXiv:0803.2706
- Verde, L., Wang, L., Heavens, A. F., & Kamionkowski, M. 2000, MNRAS, 313, 141
- Warren M.S., Abazajian K., Holz D.E., Teodoro L., 2006, ApJ, 646, 881
- White, M. 2002, ApJS, 143, 241
- Willick, J. A. 2000, ApJ, 530, 80
- Yadav, A. P. S., & Wandelt, B. D. 2008, Physical Review Letters, 100, 181301
- Zel'dovich, Y. B. 1970, AAP, 5, 84